Trap-limited carrier recombination in single-walled carbon nanotube heterojunctions with fullerene acceptor layers

Andrew J. Ferguson, Anne-Marie Dowgiallo, Dominick J. Bindl, Kevin S. Mistry, Obadiah G. Reid, Nikos Kopidakis, Michael S. Arnold, and Jeffrey L. Blackburn

Trap-limited carrier recombination in single-walled carbon nanotube heterojunctions with fullerene acceptor layers

Andrew J. Ferguson,[1,*] Anne-Marie Dowgiallo,[1] Dominick J. Bindl,[2] Kevin S. Mistry,[1] Obadiah G. Reid,[1] Nikos Kopidakis,[1] Michael S. Arnold,[2] and Jeffrey L. Blackburn[1,*]

[1] *Chemistry & Nanoscience Center, National Renewable Energy Laboratory, Golden, Colorado 80401, USA*
[2] *Department of Materials Science and Engineering, University of Wisconsin—Madison, Madison, Wisconsin 53706, USA*

Single-walled carbon nanotube (SWCNT)-fullerene (C_{60}) bilayers represent an attractive "donor-acceptor" binary system for solar photoconversion, where the kinetics of photoinduced processes depend critically on the properties of the interface between the two materials. Using photoconductivity measurements we identify the kinetic scheme that describes the free carrier kinetics in such bilayers where the dominant SWCNT species is the (7,5) semiconducting nanotube. Following charge separation, the carrier kinetics, covering up to four order of magnitude in volumetric hole density, are described by a trap-limited recombination process that is limited by capture and emission at traps or states at the SWCNT-C_{60} interface. The high frequency mobility of holes in the (7,5) SWCNT phase is lower than in multi-chiral films, potentially due to differences in SWCNT defect density for nanotubes that have been purified more aggressively. The results obtained here provide fundamental insights into the transport and recombination of both charges and excitons within SWCNT thin films and bilayers, and point to several potential ways to improve SWCNT-C_{60} photovoltaic devices.

* Corresponding Authors: andrew.ferguson@nrel.gov, jeffrey.blackburn@nrel.gov

Semiconducting single-walled carbon nanotubes (s-SWCNTs) possess optical and electrical properties that rival many of the best inorganic and organic semiconductors currently employed in photovoltaics (PVs) [1], including optical absorptivity of $>10^5$ cm^{-1} at the excitonic bandgap [2], intra-tube charge carrier mobilities exceeding 10^4 cm^2/V·s [3], and intra-tube exciton diffusion lengths of several hundreds of nanometers [4-6]. Indeed, several studies have demonstrated relatively efficient thin-film solar cells employing a Type-II heterojunction between s-SWCNTs and C$_{60}$ fullerenes, where photocurrent is driven primarily by photons absorbed in the thin (< 30 nm) SWCNT "donor" layer [7-9]. The principles of operation for such devices echo those of other bilayer organic PV devices: photons absorbed in s-SWCNTs produce correlated electron-hole pairs (excitons), which diffuse to the interface with the "acceptor" (C$_{60}$) layer, an interfacial free energy driving force induces exciton dissociation *via* fast electron transfer ($\leq$ 120 fs) from s-SWCNTs to fullerenes [1,10], and charges then migrate through each phase to the appropriate contacts where they are collected. Although significant improvements have been made in SWCNT-based PV devices, balancing this complex series of steps can make device optimization arduous and significant improvements remain to realize the full potential of SWCNT-based PV. A critical feature of donor-acceptor systems such as the one discussed here is the interface between the two materials, which is the locus of free carrier generation, but also that of recombination and trapping [11]. Despite the importance of these interfacial processes, a clear understanding is lacking. In this paper we use spectroscopic measurements that are sensitive to primary photochemical events – e.g. exciton diffusion, exciton dissociation, charge generation, and recombination – to provide unique insights into the kinetics of charge decay at the interface and discuss routes for improving charge separation in PV active layers without constructing full devices.

We have recently used the time-resolved microwave conductivity (TRMC) technique to probe charge generation and recombination in a number of organic donor-acceptor systems [2,11-13], including systems pairing SWCNTs with either semiconducting polymer electron donors [3,14,15] or fullerene electron acceptors [7-9,16]. TRMC is a time-resolved pump-probe technique that measures pump-induced charge generation through the absorbance of the microwave probe beam by mobile carriers. In both polymer-SWCNT and SWCNT-fullerene systems, TRMC reveals the presence of long-lived charges following excitation of the electron donor [14-16]. These long-lived charges result from exciton dissociation across the interface [10], such that electrons and holes separated into the two different phases experience a reduced Coulombic attraction and a correspondingly reduced rate of recombination. In the SWCNT-C$_{60}$ system, wavelength-dependent excitation of different SWCNT bandgaps revealed that the efficiency of charge generation depends sensitively on the free energy driving force for charge separation (ΔG_{CS}), which trends toward zero at a diameter of ~1.1 nm [16]. Interestingly, that study also revealed that bandgap excitation of neat s-SWCNT films produces a significant yield (~5%) of charge carriers

even in the absence of an intentional exciton dissociation interface, in agreement with previous terahertz spectroscopic measurements [17] and recent photocurrent measurements [18].

In this study, we use TRMC to probe charge generation and carrier kinetics in SWCNT/C_{60} bilayer thin films with only one major species of s-SWCNT, the (7,5) SWCNT [19]. Reducing the distribution of SWCNT species helps to simplify the energetic landscape available for exciton and charge diffusion within the SWCNT film thereby allowing us to extract, for the first time, information regarding the kinetics of charge carriers at the interface. Our results shed light on several important considerations for SWCNT/C_{60} bilayer solar cells. For a fixed absorbed photon flux, charge recombination depends sensitively on the thickness of the film, which determines the *volumetric charge density* within the SWCNT phase following exciton dissociation. By varying the photoexcitation fluence, approaching solar irradiation conditions at the lowest intensities, we are able to apply a model that considers trapping/detrapping of holes in the SWCNT layer following exciton dissociation to globally reproduce the photoconductance decay dynamics of bilayers with varying SWCNT layer thicknesses. Although the precise nature of the trapping sites in unknown at this time, we postulate that it may be related to states associated with the SWCNT-C_{60} interface or SWCNT defect states. The latter may also result in a hole mobility within the (7,5) films studied here that is significantly lower than that measured in the multi-chiral films we studied previously [16]. Our results highlight the potentially significant influence of defects/traps on carrier mobility and recombination in devices prepared with coupled semiconducting SWCNTs, and encourage further studies aimed at understanding and mitigating the source of these defects.

Figure 1(a) displays the absorbance spectrum for a ~9 nm neat (7,5) s-SWCNT film. The spectrum is primarily dominated by excitonic transitions specific to the (7,5) s-SWCNT. The first and second exciton transitions of the optically allowed "bright" exciton (S_{11} and S_{22}) appear at 1046 nm and 650 nm, respectively. Additionally, due to the high chiral purity of the sample, vibronic transitions associated with the "dark" K-momentum exciton [20-22] can easily be identified at 860 nm and 580 nm. The absorbance of the dispersing PFO polymer can be seen at 390 nm. Although ~99% of this PFO polymer is removed following the initial dispersion, the final dispersion (and thus doctor-bladed film) contains ~1:1 polymer:SWCNT by weight. Small peaks at 1150 nm and 1210 nm indicate a small percentage of minority SWCNT species, the (7,6) and (8,6) s-SWCNTs respectively, representing < 5% of all SWCNTs within the film. It is also possible that other optical transitions associated with the (7,5) s-SWCNT contribute to absorption at wavelengths beyond 1150 nm. For example, residual charges on (7,5) s-SWCNTs (e.g. from purification in strong acids) [23] could induce absorption at ~1230 nm that is associated with charged excitons (trions) [10,24,25].
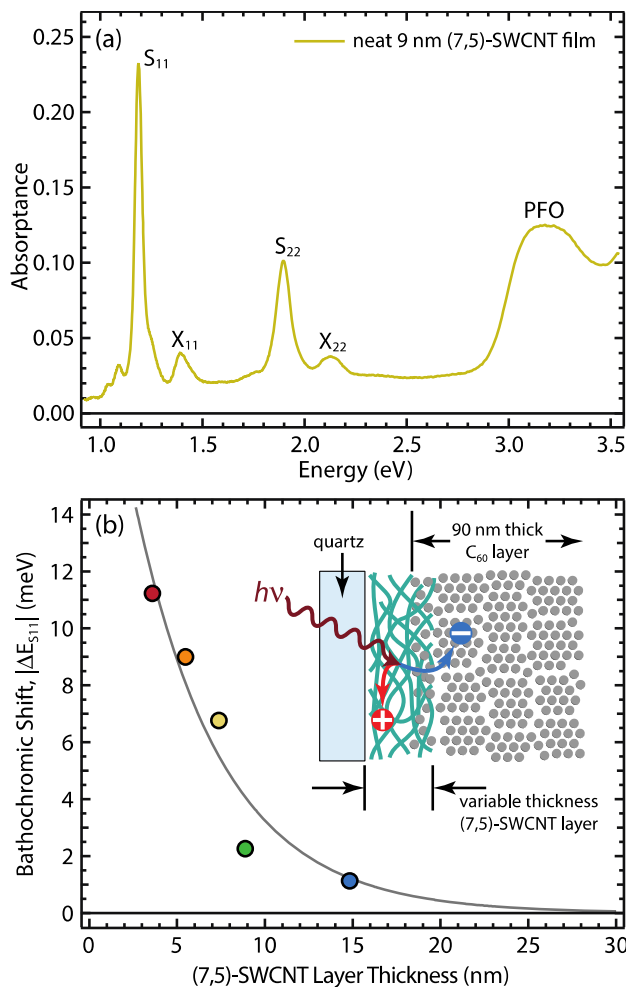
FIG. 1. (Color online) (a) Absorptance spectrum of the neat ~9 nm thick (7,5) s-SWCNT film (without C_{60}). Peaks corresponding to the first and second excitonic transitions of the (7,5) SWCNT are labeled as S_{11} and S_{22} whereas the corresponding vibronic transitions are labeled X_{11} and X_{22}. (b) Red shift of the absorbance peak associated with the S_{11} exciton induced by the C_{60} layer as a function of SWCNT film thickness. Inset: Cartoon schematic of the SWCNT/C_{60} bilayer studied by TRMC. (7,5) s-SWCNT films with varying thicknesses are deposited on quartz, after which a 90 nm C_{60} layer is thermally evaporated. Photoexcitation pulses first pass through the quartz substrate to generate SWCNT excitons.

Figure 1(b) shows the red shift of the S_{11} exciton transition for (7,5) SWCNT films with varying thickness after C_{60} has been deposited on the SWCNTs [see schematic in the inset of Fig. 1(b)]. The S_{11} exciton energy shows a large red-shift for the thinnest films, which rapidly diminishes with increasing SWCNT layer thickness. This redshift most likely arises from a change in the dielectric constant when SWCNTs are surrounded by fullerenes that intercalate into the underlying nanotube layer, in which case the magnitude of the redshift indicates a relative percentage of SWCNTs in direct contact with fullerenes.

Figure 1(b) suggests that as the SWCNT layer thickness increases, a smaller percentage of SWCNTs are in direct contact with the C_{60} acceptor phase.

The TRMC technique employed here enables direct measurement of the photoinduced free carrier population by monitoring the resulting microwave absorption by the sample ΔP, which is proportional to the high-frequency (~9 GHz) photoconductance (ΔG). The photoconductance in turn is proportional to the photo-generated free carrier yield (ϕ) and the sum of the high-frequency free carrier mobilities ($\Sigma\mu$). Thus, an often used figure-of-merit from the TRMC measurement is the peak (or end-of-pulse) yield-mobility product, $(\phi\Sigma\mu)_{EOP}$, measured at times immediately following the photoexcitation pulse, which can be used to estimate the free carrier generation yield (if mobility can be reliably estimated). The time evolution of ΔG is a direct probe of free carrier loss processes, such as recombination and/or trapping (provided the mobility is time-independent). Additional details for the TRMC method are provided in the Methods section.

Figure 2(a) displays photoconductance transients [$\Delta G(t)$] following S_{11} photoexcitation (1050 nm) of two 9 nm (7,5) SWCNT films – one with (bilayer) and one without (neat) a 90 nm C_{60} electron-accepting layer. Without the C_{60} layer, a small and rapidly decaying photoconductance signal indicates that some amount of free charge carriers result from photoexcitation of the (7,5) SWCNTs, even without an intentionally deposited exciton dissociation interface. The majority of these carriers (>90%) decay within the first 10 ns, similarly to what we observed for neat multi-chiral SWCNT thin films [16]. Addition of the C_{60} electron-accepting layer increases ΔG significantly and produces a photoconductance transient with a much longer decay than that of the neat film. In this case, 20% of the signal remains at 500 ns, indicating a significant fraction of very long carrier decay times. Both the increase of photoconductance and lengthening of the photoconductance transient are consistent with exciton dissociation at the SWCNT/C_{60} interface and an associated hindrance of charge recombination due to spatial separation of charges in the two phases [10,16].

Figure 2(b) displays a photoconductance action spectrum of the (7,5) SWCNT/C_{60} bilayer film overlaid on top of the absorptance spectrum near the S_{11} exciton transition. The photoconductance action spectrum closely matches the excitonic features of the (7,5) SWCNT absorptance, both the bright S_{11} exciton transition at ~1046 nm and the vibronic X_{11} transition [22] at 860 nm. The correlation with the vibronic sideband [also see Fig. 2(c)] is particularly interesting, since this peak originates from a transition coupling the formally optically forbidden K-momentum exciton with a D-band ($A_1{}'$) phonon [22]. The same correlation was found in recent device studies [7,26], and indicates that similar exciton densities are able to diffuse to the interface and be dissociated, regardless of the state from which they originate.
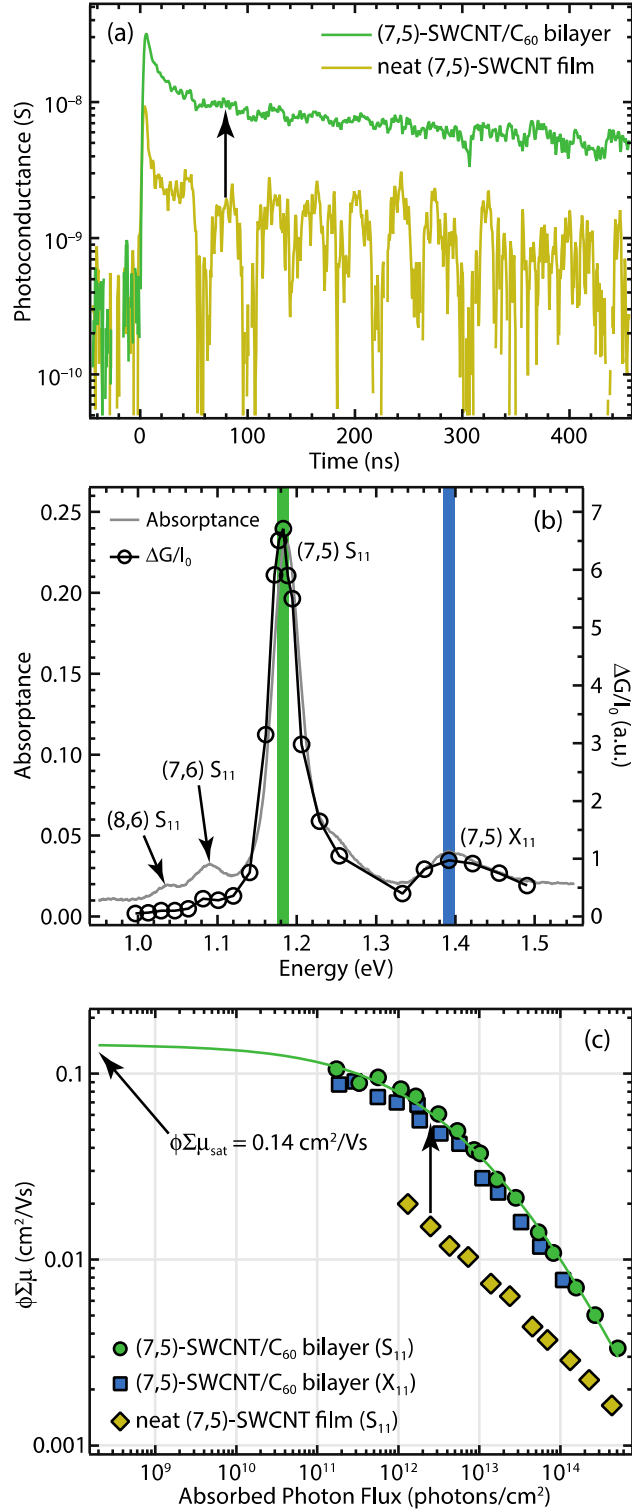
FIG. 2. (Color online) Microwave photoconductivity data for the ~ 9 nm neat and bilayer (7,5) s-SWCNT films (λ_{ex} = 1048 nm). (a) Photoconductance transients measured at an absorbed photon fluence, $I_0 F_A \approx 1 \times 10^{12}$ cm^{-2}. (b) Photoconductance action spectrum (black circles) overlaid with the SWCNT absorptance spectrum (solid grey line). (c) Fluence-dependent yield-mobility product ($\phi\Sigma\mu$): data are

shown for S_{11} (yellow-filled diamonds; λ_{ex} = 1048 nm) excitation of the neat film, and both S_{11} (green-filled circles; λ_{ex} = 1048 nm) and X_{11} (blue-filled squares; λ_{ex} = 886 nm) excitation of the bilayer film. The solid green fit line shows extrapolation of fluence-dependent $\phi\Sigma\mu$ to ~1 sun fluence, using Eq. 1.

Figure 2(c) displays the fluence dependence of the end-of-pulse photoconductivity, $(\phi\Sigma\mu)_{EOP}$, for the neat and bilayer 9 nm (7,5) films. In this case, the peak photoconductance is normalized by the absorbed photon flux, which yields a value representative of the product of free charge carrier yield and the mobility of all charges interacting with the microwave probe. At all fluences, the $(\phi\Sigma\mu)_{EOP}$ is larger for the bilayer film than that of the neat film, as expected for efficient interfacial exciton dissociation. We also note that excitation of a neat C_{60} film at 1050 nm produced negligible microwave absorbance. For both films shown in Fig. 2(c), if we assume that the carrier mobility remains constant with fluence, the carrier yield decreases with increasing photon fluence. As discussed in our previous study on SWCNT/C_{60} bilayers containing multiple SWCNT chiralities, this trend is consistent with other pump-probe measurements that find a sub-linear increase in the density of charge carriers resulting from fluence-dependent multi-body Auger processes [25].

At low absorbed photon fluences, approaching 10^{11} cm^{-2}, $(\phi\Sigma\mu)_{EOP}$ in the bilayer begins to saturate around a value of 0.1 cm^2/V·s. Assuming an exciton lifetime of ~100 ps, this fluence regime corresponds to a peak exciton density of a few tenths of an exciton per micron length of (7,5) SWCNT within the 4 ns pump pulse [16]. The green fit line in Fig. 2(c) extrapolates the fluence-dependent yield-mobility data to low fluence (~1 sun), using the empirically demonstrated [12,27] square-root dependence of photoconductance on absorbed fluence due to second-order loss processes, with a modified equation of the form [15]:

$$\phi\Sigma\mu = \frac{A}{\left(1 + \sqrt{B \cdot I_0 F_A} + C \cdot I_0 F_A\right)} \tag{1}$$

The terms A, B, and C in Eq. (1) are empirical fitting parameters, and A represents the saturation value at low fluences consistent with 1 sun AM 1.5G conditions ($\phi\Sigma\mu_{sat}$). Extrapolation *via* Eq. (1) yields a low-fluence $\phi\Sigma\mu_{sat} \approx 0.14$ cm^2/V·s for the (7,5) bilayer, which is almost an order of magnitude lower than the value obtained in our previous study of s-SWCNT/C_{60} bilayer films prepared from ~9 nm thick multi-chiral SWCNT films ($\phi\Sigma\mu_{sat} \approx 1.28$ cm^2/V·s). This result is surprising, since the internal quantum efficiencies (IQE) for mono-chiral and multi-chiral thin-film PV devices fabricated from identically prepared ~ 9 nm films suggest *higher carrier yields* for (7,5) mono-chiral films. Specifically, for devices prepared from 9 nm thick SWCNT layers, multi-chiral and mono-chiral devices have respective average IQE values of 45 ± 9% [28] and 70 ± 13% (measured for this study). Thus, the significantly lower yield-

mobility product observed for the (7,5) mono-chiral film suggests that the *high-frequency carrier mobility* within these films is appreciably lower than in multi-chiral films. Since both films employ an identical evaporated C_{60} layer as the electron-accepting phase, the electron mobility within this phase cannot be responsible for this dramatic difference. This leaves the necessary conclusion that the SWCNT hole mobility is appreciably lower in the mono-chiral (7,5) films studied here than in the previously studied multi-chiral films.

To estimate the 9 GHz (7,5) SWCNT hole mobility, we decompose $\phi\Sigma\mu_{sat}$. We assume an exciton dissociation yield of $\phi \approx 0.7$, based on the IQE discussed above and use a C_{60} electron mobility 0.01 cm^2/V·s, based on a detailed analysis from our previous study [16]. These estimates allow us to calculate a SWCNT hole mobility of ~0.2 cm^2/V·s, which is ~6 times lower than found for the ~9 nm HiPCO film in our previous TRMC study [16]. It is possible that this reduced mobility results from purification-related defects [23], since the source material for the (7,5) films undergoes rigorous acidic purification by the manufacturer. In contrast, the source material for the multi-chiral films received no purification. Potential sources for this reduced hole mobility for the (7,5) films will be explored further in a subsequent publication.

With the basic understanding of the charge generation mechanism and charge mobility, we next set out to explore the dependence of charge carrier yield and recombination kinetics on the thickness of the SWCNT donor layer. Previous device measurements provide a useful reference point, as they have demonstrated high IQE values of ~85% for very thin films (e.g. < 5 nm) [8] that *decrease* with increasing film thickness [28]. A thickness-dependent TRMC study enables us to probe the charge generation yield in the absence of charge collection that is required for functioning PV devices. Figure 3a displays the fluence-dependent $(\phi\Sigma\mu)_{EOP}$ obtained for bilayer (7,5) films ranging from ~3 to 14 nm, each containing a 90 nm C_{60} electron accepting layer. The $(\phi\Sigma\mu)_{EOP}$ can safely be used to compare thickness-dependent free carrier yields only if the following two assumptions are valid: (1) the carrier mobilities do not change appreciably with thickness, and (2) negligible carrier loss occurs during the pulse, so that the end-of-pulse photoconductance accurately captures all photogenerated carriers. Figure 3(a) shows the unexpected trend that $(\phi\Sigma\mu)_{EOP}$ *increases* with increasing SWCNT thickness, the opposite of what is expected from IQE measurements. This contradiction suggests that one, or both, of the assumptions from above is not being met.
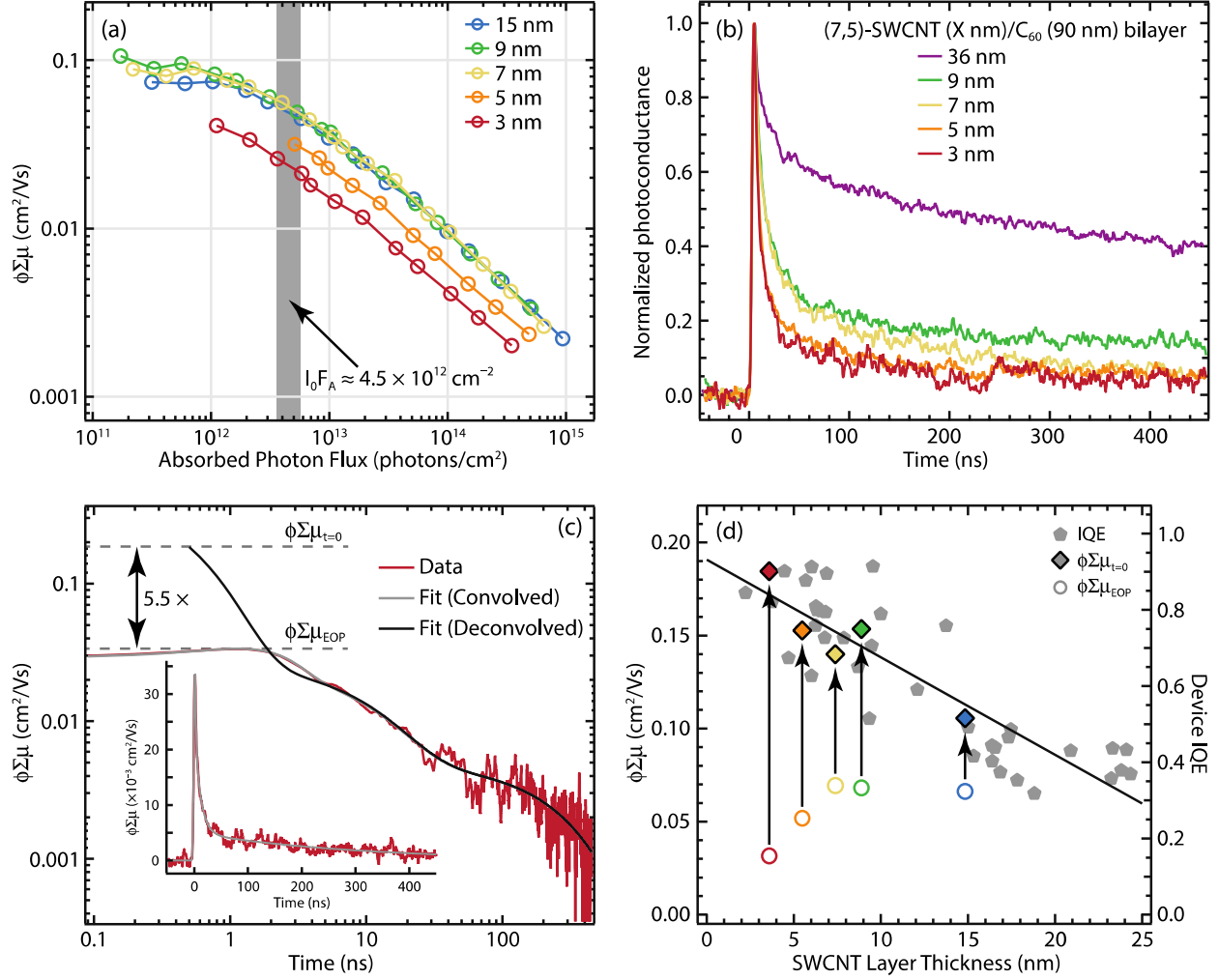
FIG. 3. (Color online) (a) Dependence of yield-mobility product ($\phi\Sigma\mu$) on absorbed photon flux (I_0F_A) for SWCNT/C_{60} bilayers with varying SWCNT thickness. (b) Normalized photoconductance (ΔG) transients for five SWCNT/C_{60} bilayers with varying SWCNT thickness, all taken at $I_0F_A \approx 4.5 \times 10^{12}$ cm^{-2} [corresponding to the grey shaded area in Fig. 3(a)]. (c) Tri-exponential fit (solid grey trace) to the 3 nm SWCNT/C_{60} bilayer transient from Fig. 3(b) (solid red trace). The solid black trace shows the extrapolation of the fit to t=0 [$(\phi\Sigma\mu)_{t=0}$] using the sum of the prefactors of the exponential terms for each time constant obtained in the fit. The dashed lines show the magnitudes of $(\phi\Sigma\mu)_{EOP}$ and $(\phi\Sigma\mu)_{t=0}$. (d) Comparison of the end-of-pulse (open circles) and t=0 (filled diamonds) yield-mobility products (left axis), along with the internal quantum efficiencies (IQE, grey pentagons) obtained for a large number of SWCNT-C_{60} PV devices utilizing identically prepared SWCNT/C_{60} bilayers.

To probe this inconsistency in more depth, we plot photoconductance transients for four (7,5) bilayer films of different thicknesses in Fig. 3(b), where each transient is taken at an approximately equal *absorbed photon flux*. It is immediately apparent that the photoconductance kinetics change dramatically

as a function of SWCNT layer thickness. The transient for the thinnest (~3 nm) film is very short-lived, with near-complete decay within the first ~250 ns. As the SWCNT thickness is increased, the transients grow longer-lived with progressively more signal intensity remaining at 500 ns. In the following analysis, we utilize two models to describe the photoconductance decay transients: (1) an *empirical* tri-exponential decay, that only provides qualitative insight about the decay processes and allows extrapolation of the decay to t = 0 (as described in more detail below); and (2) a kinetic model that includes trapping and de-trapping of holes and second-order free carrier recombination at the SWCNT-C_{60} interface. To account for the rapid carrier decay in the thinner films the photoconductance transients were first fit empirically with a tri-exponential decay convoluted with a Gaussian (~4 ns FWHM) representing the infrared pump pulse. The results of the fit for the bilayer with the ~3 nm SWCNT film are shown in Fig. 3(c). The transient is best fit with time constants of 540 ps, 10.7 ns, and 298 ns, and the 540 ps component has significantly higher amplitude than the other two components [29]. Interestingly, the values of these time constants change little with absorbed photon fluence, as shown in Fig. S1(b). Such behavior is atypical of bimolecular recombination, a consideration we return to below in the detailed kinetic model.

Most importantly, if the contribution of all photogenerated carriers is successfully captured by the empirical fit, the sum of the prefactors of the exponential terms should equal $(\phi\Sigma\mu)_{EOP}$, accounting for all recombination and trapping that occurs during the laser pulse. When we sum the three prefactors of the exponential terms extracted from the fit in Fig. 3(c), this sum is over five times higher than $(\phi\Sigma\mu)_{EOP}$. This discrepancy implies that over 80% of the photogenerated charge carriers in this very thin SWCNT/C_{60} bilayer are being lost within the pulse and are not represented appropriately by $(\phi\Sigma\mu)_{EOP}$. Extrapolating back to the value of $\phi\Sigma\mu$ at t = 0 [$(\phi\Sigma\mu)_{t=0}$], as shown in Fig. 3(c), is thus a better representation of the true carrier yield for films of different thicknesses, since this value captures carriers that are lost within the pulse due to the thickness-dependent recombination kinetics observed in Fig. 3(b). Figure 3(d) compares $(\phi\Sigma\mu)_{t=0}$ to that obtained from the peak photoconductance signal [$(\phi\Sigma\mu)_{EOP}$]. In all cases, $\phi\Sigma\mu$ is higher at t = 0 than is measured at end-of-pulse, but this increase is most dramatic for the thinnest films. The internal quantum efficiencies measured for a large number of PV devices, with varying thickness, are also plotted in Fig. 3(d). The $(\phi\Sigma\mu)_{t=0}$ values follow the same general trend as device IQE, decreasing with increasing thickness, whereas there is very poor correlation of $(\phi\Sigma\mu)_{EOP}$ with device IQE.

While the empirical tri-exponential fits give some insight into the unexpected thickness-dependent behavior, it is preferable to develop a physically relevant kinetic model that can capture the effects of thickness and excitation fluence on charge recombination dynamics. To address this challenge, we performed global fits to the photoconductance transients of the SWCNT/C_{60} bilayers using a kinetic model that includes a trap-limited recombination process [30]. We were motivated to consider the influence of charge carrier trapping by the pseudo-first order recombination kinetics observed from the

empirical tri-exponential fits [Fig. S1(b)]. Several studies on recombination in photoexcited organic PV blends have attributed pseudo-first order recombination kinetics to trap– or interface-state–mediated recombination (e.g. similar to Shockley-Read-Hall recombination in crystalline semiconductors) [31-33]. Furthermore, since Figs. 3 and S4(b) demonstrate that the carrier density within the SWCNT film dramatically affects the apparent photoconductance decay kinetics, we considered a model in which the availability of free holes (h_f) in the SWCNT layer for bimolecular recombination with free electrons (e_f) in the C_{60} layer is mediated by hole traps within the SWCNT network.

The inset of Fig. 4(b) provides a schematic of our model: in this scheme, e_f and h_f recombine at a rate described by the coefficient for bimolecular recombination at a planar interface γ_R, (units of cm^4.carrier^{-1}.s^{-1}) [34]. However, free holes may be trapped in unidentified states with a characteristic rate constant k_t. Trapped holes, h_t, are thermally "de-trapped" with a characteristic rate constant k_{dt}. The time-dependent number of free holes (in the SWCNT layer) and electrons (in the C_{60} layer) resulting from this scenario can be modeled with the following rate equations:

$$\frac{dh_f}{dt} = -k_t h_f + k_{dt} h_t - \gamma_R A \left[h_f \right] \left[e_f \right] \tag{2}$$

$$\frac{de_f}{dt} = -\gamma_R A \left[h_f \right] \left[e_f \right] \tag{3}$$

where h_f and e_f are the *number of carriers*, and $[h_f]$ and $[e_f]$ are the *volumetric carrier densities,* in the SWCNT and C_{60} layer, respectively, and A is the interfacial area. Since the TRMC experiment is only sensitive to the mobile carriers, the time-dependent photoconductance signal, $\Delta G(t)$, is given by:

$$\frac{\Delta G(t)}{\beta q_e} = \mu_h h_f(t) + \mu_e e_f(t) \tag{4}$$

where $\beta = 2.2$ (which is the ratio of the long and short dimension of the X-band waveguide used), q_e is the elementary charge, and μ_h / μ_e are the high-frequency (~9 GHz) hole/electron mobilities, respectively. We note that, in all cases, the model converges on a solution where the fastest carrier is also the one that undergoes trapping and detrapping. From this convergence, we conclude that the holes in the SWCNT layer are the primary carriers that experience trap sites, based on the fact that the high-frequency (~9 GHz) hole mobility in the SWCNT network is expected to be at least an order of magnitude larger than the electron mobility in the C_{60} layer, particularly for polycrystalline films such as those prepared using thermal evaporation. Additional details for the simulation are provided in the Supplemental Material [19].
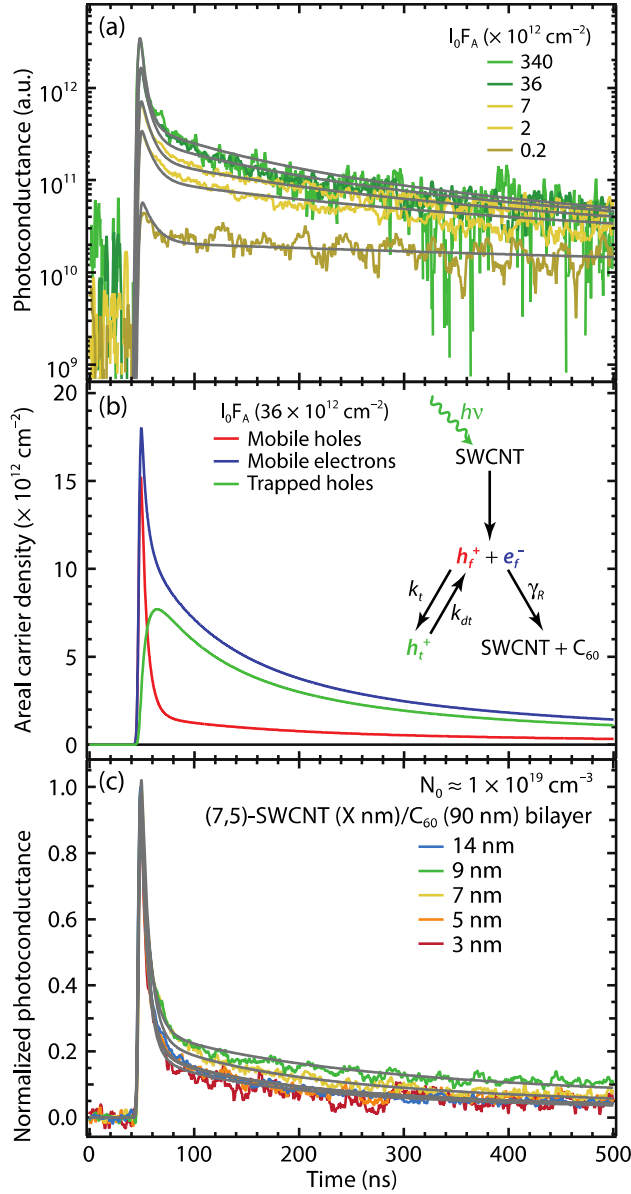
FIG. 4. (Color online) (a) Photoconductance transients for the SWCNT/C$_{60}$ bilayer with ~7 nm SWCNT layer thickness. The grey traces are photoconductance decays simulated using Eqs. 2 − 4. (b) Simulated decay trajectories of each individual carrier considered in the simulation of the transient at an absorbed photon flux of 36×10^{12} cm^{-2} in panel (a). Inset: schematic of the trap-limited recombination model used to generate the rate Eqs. 2 and 3. (c) Photoconductance transients for the SWCNT/C$_{60}$ bilayers with varying SWCNT layer thickness at an initial volumetric carrier density of ~1×10^{19} cm^{-3}. The grey traces are photoconductance decays simulated using Eqs. 2 − 4.

Figure 4(a) displays simulated photoconductance decays for the ~7 nm SWCNT bilayer at five different absorbed photon fluxes overlaid on top of the experimental transients. The best simulations in

Fig. 4(a) were obtained by adopting trapping and detrapping rate constants of $k_t = 7.3 \times 10^7$ s^{-1} and $k_{dt} =$ 2.4 $\times$ 10^7 s^{-1}, and a bimolecular recombination coefficient, $\gamma_R = 1.0 \times 10^{-16}$ cm^4.carrier^{-1}.s^{-1}. Figure 4(b) displays the modeled time-dependent trajectories of each individual species – free electrons, free holes, and trapped holes – for the transient at a photon flux of 36×10^{12} cm^{-2}. The free hole density is rapidly depleted initially due to trapping, leading to the concomitant rapid rise of the trapped hole density. After ~100 ns, an equilibrium is established between free and trapped holes, which limits the recombination of free holes with free electrons. Figure 4(c) shows simulated photoconductance decays for five SWCNT/C$_{60}$ bilayer samples with varying SWCNT layer thickness, at an initial volumetric carrier density (N_0) of ~1 $\times$ 10^{19} cm^{-3}. This comparison indicates both that the model is capable of fitting the transient data as a function of the SWCNT layer thickness and that the photoconductance decay kinetics are similar for *identical initial carrier densities*. It is interesting to note that the second-order bimolecular recombination coefficient appears to decrease with increasing film thickness (with the exception of the sample with the 14.8 nm thick SWCNT layer). We attribute this decrease to a subtle increase in the amount of time taken for holes to reach the interface between the SWCNT and C$_{60}$ layers, where the recombination event takes place. Because the interface between these two materials is likely to be blurred [c.f. the red-shifted S$_{11}$ absorption transition in Fig. 1(b)] the γ_R value for the sample with the 3.6 nm thick SWCNT layer likely represents an 'intrinsic' rate coefficient for the second-order recombination process, since the holes should not have to diffuse to encounter electrons at the interface.

TABLE I. Fit parameters extracted from global analysis of the photoconductance transients for bilayer samples with varying SWCNT layer thicknesses

SWCNT layer thickness (nm)	γ_R ($\times$ 10^{-16} cm^4.carrier^{-1}.s^{-1})	k_t ($\times$ 10^7 s^{-1})	k_{dt} ($\times$ 10^7 s^{-1})	μ_h (cm^2/V·s)	μ_e (cm^2/V·s)
3.6	2.62				
5.5	2.27				
7.4	1.00	7.33	2.40	0.097	0.01
8.9	0.59				
14.8	1.84				

The close match of the simulations to the fluence-dependent transients indicates that a simple model, in which reasonably fast bimolecular recombination is limited by a relatively slow trapping/de-trapping event, can accurately reproduce the photoconductance decays. This is particularly striking, since the model does not need to account for either spatial or energetic distributions of the trap states to provide good fits over up to four orders of magnitude in absorbed photon flux. Figure S5 demonstrates that the same model is also able to simulate photoconductance decays from bilayers containing the full range of SWCNT layer thickness. From these simulations, we conclude that hole traps within the thin SWCNT layer may play a crucial role in determining the rate of interfacial recombination of electrons and holes

across the SWCNT/C_{60} interface. The chemical/physical identity of these trap states is currently unclear, but we can conjecture a variety of potential sources for the traps: dangling bonds at open ends of SWCNTs [35,36], sidewall defects, potential wells at the junctions between SWCNTs or the interfaces between a SWCNT and the wrapping polymer, or states at the SWCNT-C_{60} interface.

In conclusion, we utilize time-resolved microwave conductivity as a sensitive optical probe of free carrier generation and recombination in (7,5) s-SWCNT/C_{60} bilayer films that are representative of thin-film PV active layers. Following excitation of both excitonic and vibronic transitions, interfacial exciton dissociation in such bilayers creates long-lived charges. The apparent recombination kinetics and charge carrier yield depend sensitively upon the thickness of the SWCNT layer and the resulting volumetric carrier within this layer. After accounting for rapid carrier loss processes, the thickness-dependent free carrier yield measured by TRMC tracks the IQE of devices with different SWCNT layer thicknesses. The successful reconstruction of photoconductance decay kinetics by a model based on a trap-limited free carrier recombination suggests that trap states within the SWCNT layer or at the nanotube-fullerene interface are important to consider for SWCNT-C_{60} PV devices. Reduced hole mobility in near-mono-chiral (7,5) s-SWCNT films, relative to previously studied multi-chiral s-SWCNT films, may also be related to defect states with similarly unknown origin. Future studies aimed at understanding and mitigating the source of these trap states may elucidate their role in the operation of thin-film SWCNT-based devices, such as solar cells, detectors, and field-effect transistors, and suggest strategies to enhance the device performance.

[1]   M. S. Arnold, J. L. Blackburn, J. J. Crochet, S. K. Doorn, J. G. Duque, A. Mohite, and H. Telg, Phys. Chem. Chem. Phys. **15**, 14896 (2013).
[2]   M.-Y. Wu, R. M. Jacobberger, and M. S. Arnold, J. Appl. Phys. **113**, 204504 (2013).
[3]   T. Durkop, S. Getty, E. Cobas, and M. Fuhrer, Nano Lett. **4**, 35 (2004).
[4]   S. Moritsubo, T. Murai, T. Shimada, Y. Murakami, S. Chiashi, S. Maruyama, and Y. K. Kato, Phys. Rev. Lett. **104**, 247402 (2010).
[5]   J. J. Crochet, J. G. Duque, J. H. Werner, B. Lounis, L. Cognet, and S. K. Doorn, Nano Lett. **12**, 5091 (2012).
[6]   A. Ishii, M. Yoshida, and Y. K. Kato, Phys. Rev. B **91**, 125427 (2015).
[7]   D. J. Bindl, M.-Y. Wu, F. C. Prehn, and M. S. Arnold, Nano Lett. **11**, 455 (2011).
[8]   D. J. Bindl and M. S. Arnold, J. Phys. Chem. C **117**, 2390 (2013).
[9]   M. J. Shea and M. S. Arnold, Appl. Phys. Lett. **102**, 243101 (2013).
[10] A.-M. Dowgiallo, K. S. Mistry, J. C. Johnson, and J. L. Blackburn, ACS Nano **8**, 8573 (2014).

[11] A. J. Ferguson, J. L. Blackburn, and N. Kopidakis, Mater. Lett. **90**, 115 (2013).
[12] A. J. Ferguson, N. Kopidakis, S. E. Shaheen, and G. Rumbles, J. Phys. Chem. C **115**, 23134 (2011).
[13] T. J. Savenije, A. J. Ferguson, N. Kopidakis, and G. Rumbles, J. Phys. Chem. C **117**, 24085 (2013).
[14] A. J. Ferguson, J. L. Blackburn, J. M. Holt, N. Kopidakis, R. C. Tenent, T. M. Barnes, M. J. Heben, and G. Rumbles, J. Phys. Chem. Lett. **1**, 2406 (2010).
[15] J. M. Holt, A. J. Ferguson, N. Kopidakis, B. A. Larsen, J. Bult, G. Rumbles, and J. L. Blackburn, Nano Lett. **10**, 4627 (2010).
[16] D. J. Bindl, A. J. Ferguson, M.-Y. Wu, N. Kopidakis, J. L. Blackburn, and M. S. Arnold, J. Phys. Chem. Lett. **4**, 3550 (2013).
[17] M. C. Beard, J. L. Blackburn, and M. J. Heben, Nano Lett. **8**, 4238 (2008).
[18] Y. Kumamoto, M. Yoshida, A. Ishii, A. Yokoyama, T. Shimada, and Y. K. Kato, Phys. Rev. Lett. **112**, 117401 (2014).
[19] See Supplemental Material at http://link.aps.org/supplemental/doi for extended presentation of the sample preparation and experimental characterization.
[20] O. N. Torrens, M. Zheng, and J. M. Kikkawa, Phys. Rev. Lett. **101**, 157401 (2008).
[21] P. M. Vora, X. Tu, E. J. Mele, M. Zheng, and J. M. Kikkawa, Phys. Rev. B **81**, 155213 (2010).
[22] J. L. Blackburn, J. M. Holt, V. M. Irurzun, D. E. Resasco, and G. Rumbles, Nano Lett. **12**, 1398 (2012).
[23] J. L. Blackburn, T. J. McDonald, W. K. Metzger, C. Engtrakul, G. Rumbles, and M. J. Heben, Nano Lett. **8**, 1047 (2008).
[24] R. Matsunaga, K. Matsuda, and Y. Kanemitsu, Phys. Rev. Lett. **106**, 037404 (2011).
[25] B. Yuma, S. Berciaud, J. Besbas, J. Shaver, S. Santos, S. Ghosh, R. B. Weisman, L. Cognet, M. Gallart, M. Ziegler, B. Hönerlage, B. Lounis, and P. Gilliot, Phys. Rev. B **87**, 205412 (2013).
[26] S. L. Guillot, K. S. Mistry, A. D. Avery, J. Richard, A.-M. Dowgiallo, P. F. Ndione, J. van de Lagemaat, M. O. Reese, and J. L. Blackburn, Nanoscale **7**, 6556 (2015).
[27] G. Dicker, M. de Haas, L. Siebbeles, and J. Warman, Phys. Rev. B **70**, 045203 (2004).
[28] D. J. Bindl, M. J. Shea, and M. S. Arnold, Chem. Phys. **413**, 29 (2013).
[29] We have attempted numerous simulations to determine the minimum time constant we can extract with confidence from our photoconductance transients. When we convolve a 4 ns Gaussian pulse with a multi-exponential decay, the minimum time constant we can simulate is ~400 ps, or ~1/10 of the pulse width. The 540 ps time constant extracted from the fit shown in Fig. 3(c) approaches this lower limit, but is still within the range of a meaningful fit. Standard deviations in the fit parameters obtained from the properly weighted fits are all less than 2%, leading to propagated errors in the pre-factors of the exponential terms of ~1.5%. This means that the error bars for the filled diamonds in Fig. 3(d) are smaller than the size of the diamonds themselves.
[30] We have explored simple kinetic models based only on second-order carrier recombination at the donor-acceptor interface (i.e. that ignore carrier (hole) trapping/de-trapping processes). These models were unable to describe the intensity-dependent photoconductivity transients, particularly for the long-lived component of the decay.
[31] R. A. Street, M. Schoendorf, A. Roy, and J. H. Lee, Phys. Rev. B **81**, 205307 (2010).
[32] S. R. Cowan, A. Roy, and A. J. Heeger, Phys. Rev. B **82**, 245207 (2010).
[33] R. A. Street, Phys. Rev. B **84**, 075208 (2011).
[34] R. A. Marcus, J. Phys. Chem. **94**, 1050 (1990).
[35] S. Cambre, B. Schoeters, S. Luyckx, E. Goovaerts, and W. Wenseleers, Phys. Rev. Lett. **104**, 207401 (2010).
[36] J. A. Fagan, J. Y. Huh, J. R. Simpson, J. L. Blackburn, J. M. Holt, B. A. Larsen, and A. R. H. Walker, ACS Nano **5**, 3943 (2011).